

The Double-Burst Nature and Early Afterglow Evolution of Long GRB 110801A

QIU-LI WANG  ^{1,2} HAO ZHOU  ¹ YUN WANG  ¹ JIA REN  ¹ ZHI-PING JIN  ^{1,2} AND DA-MING WEI  ^{1,2}

¹ *Purple Mountain Observatory, Chinese Academy of Sciences, Nanjing 210023, China*

² *School of Astronomy and Space Science, University of Science and Technology of China, Hefei 230026, China*

ABSTRACT

We present a comprehensive temporal and spectral analysis of the long-duration gamma-ray burst GRB 110801A, utilizing multi-band data from the Neil Gehrels Swift Observatory and ground-based telescopes. The γ -ray emission exhibits a distinct two-episode (“double-burst”) structure. Rapid follow-up observations in the optical and X-ray bands provide full coverage of the second burst. The optical light curve begins to rise approximately 135 s after the trigger, significantly preceding the second emission episode observed in X-rays and γ -rays at ~ 320 s. This chromatic behavior suggests different physical origins for the optical and high-energy emissions. Joint broadband spectral fitting (optical to γ -rays) during the second episode reveals that a two-component model, consisting of a power-law plus a Band function, provides a superior fit compared to single-component models. We interpret the power-law component as the afterglow of the first burst (dominating the optical band), while the Band component is attributed to the prompt emission of the second burst (dominating the high-energy bands). A physical synchrotron model is also found to be a viable candidate to explain the high-energy emission. Regarding the afterglow, the early optical light curve displays a sharp transition from a rise of $\sim t^{2.5}$ to $\sim t^{6.5}$, which is well-explained by a scenario involving both reverse shock (RS) and forward shock (FS) components. We constrain the key physical parameters of the burst, deriving an initial Lorentz factor $\Gamma_0 \sim 60$, a jet half-opening angle $\theta_j \sim 0.09$, and an isotropic kinetic energy $E_{k,iso} \sim 10^{54.8}$ erg.

Keywords: Gamma-ray bursts (629)

1. INTRODUCTION

Gamma-ray bursts (GRBs) represent the most energetic explosions in the universe that originated from either the collapse of massive stars (T. Piran 2005; S. Woosley & J. Bloom 2006) or the merger of compact binaries (B. P. Abbott et al. 2017). Following a catastrophic event, an outflow is powered by the central engine and is likely collimated into a relativistic jet during propagation (O. S. Salafia & G. Ghirlanda 2022). The nature of prompt emission can be explained by the energy dissipation in the internal shock (M. J. Rees & P. Meszaros 1994; S. Kobayashi et al. 1997; J. Elliott et al. 2014) or magnetic dissipation (P. Beniamini & J. Granot 2016; J. Granot 2016; E. Troja et al. 2017), although its complex radiation mechanisms remain poorly understood. The most natural candidate is synchrotron radiation generated from energetic electrons. However, the theoretical synchrotron spectrum predicts photon indices $\alpha \sim -1.5$ in lower energy band expected for the fast cooling synchrotron model are softer than typical photon indices ($\bar{\alpha} \sim -1$), which is the so-called fast cooling problem (G. Ghisellini et al. 2000). To reconcile this inconsistency, several modifications to the canonical synchrotron framework have been suggested, such as additional inverse Compton scattering (E. Nakar et al. 2009; F. Daigne et al. 2011) or a decaying magnetic field (A. Pe’er & B. Zhang 2006; Z. L. Uhm & B. Zhang 2014; X. Zhao et al. 2014). Another alternative interpretation is the presence of a sub-dominant quasi-thermal component (in addition to a non-thermal component) (S. Guiriec et al. 2011; F.-K. Peng et al. 2014; V. Valan & J. Larsson 2021; Q.-L. Wang et al. 2025). The afterglow is powered by synchrotron radiation from the

external forward shock or reverse shock, produced as the jet interacts with the circumburst medium (P. Mészáros & M. J. Rees 1997, 1999; R. Sari & T. Piran 1999; C. H. Blake et al. 2005; B. Gendre et al. 2012; M. Arimoto et al. 2024; H. Wang et al. 2025).

The prompt emission of GRB 110801A in γ -ray shows two comparable energetic episodes separated by a quiescence time of roughly 200 s like GRB 240529A (T.-R. Sun et al. 2024). The optical observation starts during the γ -ray's quiescent time and shows a sharp rise. The two isolated γ -ray episodes and the sharp transition in the optical rise imply the presence of "refreshed shock". The "refreshed shock" scenario is commonly invoked to explain the re-brightening behavior observed in late-time afterglows (G. P. Lamb et al. 2020; M. J. Moss et al. 2023; G. Schroeder et al. 2024). In this paper, we report the analysis of long GRB 110801A data obtained by the Neil Gehrels *Swift* (N. Gehrels et al. 2004). Following the approach of Z.-P. Jin et al. (2023) and H. Zhou et al. (2023), we split the ultraviolet/optical telescope (UVOT, P. W. A. Roming et al. 2005) data taken in the event mode into finer time bins. This allowed us to investigate the optical temporal behavior during the early stage of the burst. We conclude the optical flux is dominated by the earlier shock's afterglow emission, while the X-ray and γ -ray flux is dominated by the later shell's prompt emission.

Here we present the observations and the reduction of the data described in Sec 2. The analysis of prompt emission and broadband spectral fitting results are detailed in Section 3, while the afterglow analysis is addressed in Section 4. We conclude with a summary and discussion in Section 5. The standard cosmology model with $H_0 = 67.4 \text{ km s}^{-1}\text{Mpc}^{-1}$, $\Omega_M = 0.315$ and $\Omega_\Lambda = 0.685$ (Planck Collaboration et al. 2020) is adopted in this paper. All errors are given at the 1σ confidence level unless otherwise stated.

2. OBSERVATIONS AND DATA REDUCTIONS

2.1. *Observations*

At 19:49:42 UT on August 01, 2011 (T_0), GRB 110801A triggered The *Swift* burst alert telescope (BAT, S. D. Barthelmy et al. 2005; M. de Pasquale et al. 2011). Based on the BAT location, *Swift* immediately slewed to the source and initiated follow-up observations. Then the X-ray telescope (XRT, D. N. Burrows et al. 2005) began observing the field at 19:51:21.9 UT, 99 seconds after the BAT trigger. XRT found a bright, uncatalogued X-ray source located at RA = 05h 57m 43.36s, DEC = $+80^\circ 57' 17.2''$ (J2000) with a 90% uncertainty of $4.9''$. UVOT began to observe the field of GRB 110801A about 108 seconds after the BAT trigger in the event mode. In addition, the afterglow counterpart of GRB 110801A was observed with the 10.4m GTC telescope revealing a continuum spectrum and narrow absorption lines, with a likely redshift of 1.858 (A. Cabrera Lavers et al. 2011). The burst was also detected by Konus-Wind (T. Sakamoto et al. 2011). Since the Konus-Wind observed this GRB in the waiting mode, they only have 3 channel spectral data for the Konus-Wind which cover the energy range from 20 keV to 1.2 MeV. The wide energy ranges of BAT(15 keV to 150 keV) and Konus-Wind show that the time-averaged spectrum from $T_0 - 26$ s to $T_0 + 65$ s and from $T_0 + 332$ s to $T_0 + 389$ s include two time-separated episodes are best fit with a power-law with exponential cutoff model:

$$\frac{dN}{dE} \sim E^\alpha \exp \left[-(2 + \alpha) \frac{E}{E_{\text{peak}}} \right] \quad (1)$$

The best fit spectral parameters are: $\alpha = -1.7_{-0.2}^{+0.1}$ and $E_{\text{peak}} = 140_{-60}^{+900}$ keV. The energy fluence in the 15-1200 keV band calculated by a power-law with exponential cutoff model is $7.3_{-0.9}^{+1.7} \times 10^{-6} \text{ erg/cm}^2$. The best fit spectral parameters for the Band model fixing $\beta = -2.5$ are: $\alpha = -1.70_{-0.15}^{+0.22}$, and $E_{\text{peak}} = 140_{-50}^{+1270}$ keV. The isotropic energy E_{iso} from 1 keV to 10 MeV band is $1.0_{-0.2}^{+0.3} \times 10^{53}$ erg, using the Band spectrum model.

Furthermore, the optical three color (g, Rc and Ic) CCD camera attached to the Murikabushi 1m telescope of Ishigakijima Astronomical Observatory observed the field of GRB 110801A on 19:53:51 UT, about 4 min after the BAT trigger and obtained a series of images with exposure time of 60 seconds (D. Kuroda et al. 2011).

2.2. *Data reduction*

We employed the HEASoft software package (version 6.35) to reduce the data obtained from *Swift* BAT, XRT and UVOT. The BAT light curve (15 - 350 keV) from $T_0 - 100$ s to $T_0 + 900$ s was extracted with a time bin size of 1 s and generated using standard procedures described in the *Swift*/BAT software guide³. The XRT source and background

³ <https://www.swift.ac.uk/analysis/bat/index.php>

spectral files in both PC and WT modes the redistribution matrix, and ancillary response files were reduced with the online *Swift*/XRT data products generator⁴(P. A. Evans et al. 2007; P. A. Evans et al. 2009). UVOT observed GRB 110801A in the V, B, U, W1 and WHITE bands for several epochs. For data taken in the image mode, we started from the level 2 UVOT products and made photometry with the standard aperture. For the WHITE-band and U-band data taken in the event mode, a fixed time bin of 50 s (20 s) were applied to extract the light curve in the WHITE (U) band. The standard aperture is also adopted to make photometries of the event data. The UVOT photometries are listed in Table 2

3. PROMPT EMISSION ANALYSIS

3.1. *Broadband lightcurves of the prompt emission*

As shown in Figure 1, the *Swift* BAT (15–350 keV) light curve exhibits two groups of several peaks from $T_0 - 50$ s to $T_0 + 80$ s and $T_0 + 320$ s to $T_0 + 400$ s with a quiescent period (SNR < 3) at $\sim 100 - 300$ s. Initially, we interpret the first burst as a precursor emission, as it is common to observe a weaker precursor followed by a quiescent period preceding the main burst (T. M. Koshut et al. 1995; D. Burlon et al. 2008; Y.-D. Hu et al. 2014). However, the peak flux of the first burst is comparable to that of the second, and the duration of the first burst is even longer than that of the second. These facts compel us to abandon this interpretation. These episodes have similar activity amplitudes, which would correspond to cases such as the double burst GRB 110709B (B.-B. Zhang et al. 2012) or the two-shock burst GRB 240529A(T.-R. Sun et al. 2024). Thus, the first group of BAT peaks represents the prompt emission of the burst, while the second corresponds to the second burst. The XRT shows three peaks at $\sim T_0 + 340$ s, $\sim T_0 + 355$ s, $\sim T_0 + 380$ s, then a steep decay closely traces the γ -ray light curve following the brightest one at $\sim T_0 + 380$ s. The WHITE band light curve binned with 50 s begins to rise at $T_0 + 135$ s followed by the U band light curve binned with 20 s begins a steeper rise at $T_0 + 278$ s. Furthermore, the optical data in the g, Rc and Ic band also exhibit similar behavior with a time bin of 60 s simultaneously. The high temporal-resolution optical data clearly delineate the optical evolution, revealing an abrupt change in optical rise that occurs at $\sim T_0 + 278$ s. The brightest optical peak occurs at $\sim T_0 + 378$ s in the U band, then shows a normal decay or even a plateau that does not follow X-ray or γ -ray data. The optical emission precedes the X-ray and γ -ray emission, with an initial rise at $T_0 + 135$ s compared to the delayed rise in the XRT and BAT data at $\sim T_0 + 320$ s, which implies that they may have different origins.

3.2. *Spectral analysis of the prompt emission*

The joint spectral fitting, including XRT (0.3 - 10 keV), BAT (15 - 150 keV) and optical data, was performed with XSPEC (version 12.15.0). We sliced the second prompt emission epoch into 5 time intervals aligned with the optical observation intervals (especially simultaneous optical data in g, Rc and Ic band): $T_0 + 249$ s to $T_0 + 309$ s, $T_0 + 319$ s to $T_0 + 379$ s, $T_0 + 389$ s to $T_0 + 449$ s, $T_0 + 601$ s to $T_0 + 661$ s, $T_0 + 670$ s to $T_0 + 900$ s. Given the suboptimal SNR of less than 3 in the XRT data from $T_0 + 670$ s to $T_0 + 770$ s, we extend the time interval to $T_0 + 900$ s to ensure enough SNR and the optical flux represents the mean flux during this time interval, obtained by linear interpolation. We jointly fit broadband data with the χ^2 statistic and model comparison was quantified with the Bayesian information criterion (BIC) (G. Schwarz 1978). Four models with Galactic absorption (*tbabs*) and host galaxy (*ztbabs*) absorption were used here for spectral fitting in X-ray and γ -ray bands, including power-law (PL), power-law with blackbody (PL+BB), power-law with Band model (PL+Band) and power-law with synchrotron model (PL+SYN). The cut energy of the CPL model is poorly constrained in BAT energy range. Hence, the PL model is adopted to fit the data instead of CPL. The Galactic equivalent hydrogen column density N_H is fixed as 8.22×10^{20} cm $^{-2}$ (R. Willingale et al. 2013). Given the distinct onset times of the optical and X-ray/ γ -ray emissions, we infer that they arise from different physical origins. Consequently, we attempt to employ a two-component model to disentangle their respective contributions to the spectrum. A GRB spectrum can usually be fit with a smoothly joint broken power law known as the Band function (D. Band et al. 1993) and the traditional model: a non-thermal component with a quasi-thermal component is considered. Given that synchrotron radiation is a natural candidate for the prompt emission mechanism, we also consider this possibility and discuss it in detail in the following section. For optical data, the Milky Way extinction model with $E(B-V)_{\text{MW}} = 0.0693$ (E. L. Fitzpatrick 1999) and $R_V = 3.08$ is adopted. The extinction model of Small Magellanic Cloud model and $R_V = 2.93$ is adopted for the host galaxy. When fitting the PL+Band and PL+SYN models, we observed that the low-energy spectral index of the Band function and SYN model are strongly coupled

⁴ https://www.swift.ac.uk/burst_analyser/

with the equivalent hydrogen column density of the host galaxy $N_{\text{H,host}}$ in the soft X-rays and the power-law index in the optical band. Consequently, we fixed these parameters: (1) $N_{\text{H,host}} = 4.9 \times 10^{21} \text{ cm}^{-2}$ (2) power-law index $\beta = 2$ according to the fitting result of late-time ($> T_0 + 4000 \text{ s}$) averaged XRT spectrum mentioned below, assuming no significant spectral evolution of the afterglow component.

Furthermore, we analyzed the BAT (15 – 350 keV) light curve of GRB 110801A from $T_0 + 320 \text{ s}$ to $T_0 + 400 \text{ s}$ (binned at 0.01 s) using the continuous wavelet transform method⁵ introduced by G. Vianello et al. (2018). This analysis resulted in a minimum variability timescale of $t_{\text{mvts}} \sim 1.51 \text{ s}$. Adopting this value, we then constrained the Lorentz factor Γ in this period and the minimum emission radius R_c following the formalism of V. Z. Golkhou et al. (2015):

$$\Gamma \gtrsim 110 \left(\frac{L_\gamma}{10^{51} \text{ erg s}^{-1}} \frac{1+z}{t_{\text{mvts}}/0.1 \text{ s}} \right)^{1/5} \quad (2)$$

where $L_\gamma \sim 1.7 \times 10^{51} \text{ erg s}^{-1}$ is the γ -ray luminosity (1 - 10^4 keV) according to the Konus-Wind fit results and

$$R_c \simeq 7.3 \times 10^{13} \left(\frac{L_\gamma}{10^{51} \text{ erg s}^{-1}} \right)^{2/5} \left(\frac{t_{\text{mvts}}/0.1 \text{ s}}{1+z} \right)^{3/5} \text{ cm.} \quad (3)$$

We found $\Gamma \gtrsim 88$ and $R_c \simeq 2.6 \times 10^{14} \text{ cm}$ for GRB 110801A in this period, which is consistent with the typical value $\sim 10^{14} \text{ cm}$ in V. Z. Golkhou et al. (2015) for long-duration GRBs.

3.3. Synchrotron Model

Since there is no synchrotron model available in XSPEC, we incorporated the synchrotron model from J. M. Burgess et al. (2020) into our analysis by utilizing a table model. We consider the evolution of the electron distribution function

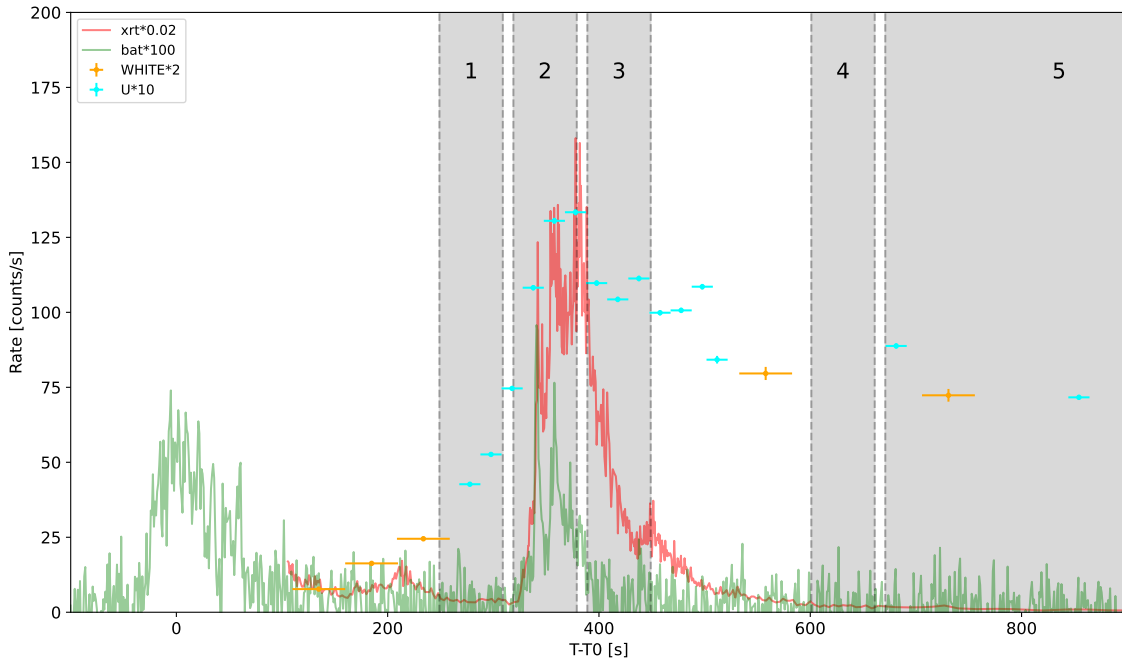


Figure 1. Multi-band emission light curves of GRB 110801A. Data are collected by *Swift* BAT (green), XRT (red), and UVOT. Note that the WHITE-band data are in orange and U-band data are in cyan. The vertical dashed lines represent the start and end times of the intervals selected for the spectral analysis.

⁵ <https://github.com/giacomov/mvts>

under synchrotron cooling alone obeys a Fokker–Planck-type equation:

$$\frac{\partial}{\partial t} n_e(\gamma, t) = \frac{\partial}{\partial \gamma} C(\gamma) n_e(\gamma, t) + Q(\gamma) \quad (4)$$

where $Q(\gamma)$ are a population of electrons accelerated into a PL energy distribution $\propto \gamma^{-p}$ for Lorentz factors γ between a minimum value γ_{\min} and a maximum value γ_{\max} with a constant index p and are cooled via emission of synchrotron photons:

$$C(\gamma) = -\frac{\sigma_T B^2}{6\pi m_e c} \gamma^2 \quad (5)$$

where σ_T is the Thomson cross-section, m_e the mass of an electron, c the speed of light, and B is the magnetic field strength. The total emission is characterized by seven parameters: Γ , B , γ_{\min} , γ_c , γ_{\max} , p and normalization. Following J. M. Burgess et al. (2020), we fix $\gamma_{\min} = 10^5$ and $\Gamma = 88$. We generate synchrotron spectra by varying $p \in [2, 6]$, $B \in [0.01, 100]$ G, $\gamma_c \in [10^{-2}, 10^2] \gamma_{\min}$ (covering slow/fast cooling), and $\gamma_{\max} \in [10^2, 10^3] \gamma_{\min}$ to ensure high-energy cutoffs above the BAT window. The synchrotron model was implemented in XSPEC in the form of a tabulated additive model.

3.4. Spectral Results and Model Comparison

As shown in Figure 2(a), the X-ray to γ -ray SEDs exhibit clear excesses in the 2–10 keV range when fitted with a simple power-law (PL) model. These excesses can be adequately described by a thermal component or a non-thermal Band component. Additionally, the PL model yields a poor fit when extrapolated to the optical band. Compared to the single-component PL model, our joint spectral fitting reveals that two-component models employing PL+BB or PL+Band provide significantly better fits during the active phases of the X-ray and γ -ray emission. However, resolving the additional spectral component is challenging during the quiescent phases ($T_0 + 601$ s to $T_0 + 661$ s and $T_0 + 670$ s to $T_0 + 900$ s) due to its weak contribution. Specifically, for the interval $T_0 + 601$ s to $T_0 + 661$ s, the cutoff energy (E_{cut}) in the PL+Band model evolves below the lower threshold of the XRT, resulting in a degeneracy between the low-energy spectral index and the dust extinction $E(B - V)_{\text{host}}$ in the optical band. Consequently, we fixed $E(B - V)_{\text{host}} = 0.106$ (the average of the three preceding epochs) to effectively constrain the Band model. For the interval $T_0 + 670$ s to $T_0 + 900$ s, the photon index of the PL component becomes similar to that of the late-time afterglow, making it difficult to disentangle the second component. Furthermore, we tested a physical synchrotron model (PL+SYN) to fit the multi-band data. Apart from the interval 319–379 s, the PL+Band model yields a fit only slightly superior to that of the PL+SYN model. Notably, the PL+SYN model provides a substantially better fit than the single PL model during the second active phase, indicating that synchrotron radiation is a viable candidate for observed X-ray and γ -ray emissions.

Table 1 details the spectral parameters and BIC statistics for the PL, PL+Band, PL+BB, and PL+SYN models. The PL+Band model generally outperforms the PL+BB model, with the exception of the interval from $T_0 + 249$ s to $T_0 + 309$ s. During this specific period, the Blackbody temperature falls within the γ -ray band, leaving the X-ray spectrum dominated by the power-law component; thus, the PL+BB fit becomes virtually indistinguishable from the single PL model. Overall, the PL+Band model not only yields better BIC statistics but also offers a more physically consistent explanation for the excess emission. In the PL+BB scenario, the excess relative to the power-law is confined to the X-ray band, implying that the optical and γ -ray emissions share a common origin (the PL component). This contradicts the behavior of the light curve, which suggests that the X-ray and γ -ray emissions likely originate from the same component. In contrast, in the PL+Band model, the Band component accounts for the excess in both the X-ray and γ -ray bands, while the optical emission is dominated by the PL component. This interpretation aligns well with the temporal evolution observed in the light curves.

Furthermore, the evolution of $E(B - V)_{\text{host}}$ derived from the PL+BB fitting shows an unphysical increase over time before decreasing. In contrast, the $E(B - V)_{\text{host}}$ derived from the PL+Band model remains constant within the error margins before dropping to the late-time afterglow level. While a decrease in $E(B - V)_{\text{host}}$ is naturally explained by dust destruction due to high-energy UV radiation (T. Komesh et al. 2023), an increase lacks a reasonable physical interpretation, further favoring the PL+Band model. Incorporating the double-burst hypothesis, we attribute the PL component to the afterglow of the first burst (dominating the optical band) and the Band component to the second burst's prompt emission (dominating the X-ray and γ -ray bands).

Although the statistical performance of the PL+SYN model is slightly inferior to that of the PL+Band model, it is also worth noting that the PL+SYN model exhibits spectral behavior consistent with that of the PL+Band model.

By interpreting the second burst's prompt emission within the synchrotron framework, we conclude that the X-ray and γ -ray flux likely originate from slow-cooling synchrotron emission during the second active phase.

Model	Parameters	Episode 1	Episode 2	Episode 3	Episode 4	Episode 5
Time range (from T_0)	Start time (s) End time (s)	249 309	319 379	389 449	601 661	670 900
Powerlaw+Band	α	$0.30^{+0.29}_{-0.40}$	$-0.03^{+0.12}_{-0.12}$	$-0.71^{+0.20}_{-0.15}$	$0.26^{+0.34}_{-0.44}$	
	β	$-1.66^{+0.09}_{-0.09}$	$-1.98^{+0.03}_{-0.04}$	$-2.05^{+0.06}_{-0.06}$	$-3.77^{+0.44}_{-0.41}$	
	E_{cut} (keV)	$0.54^{+0.17}_{-0.08}$	$2.97^{+0.48}_{-0.36}$	$1.70^{+0.41}_{-0.41}$	$0.06^{+0.02}_{-0.01}$	
	K_{Band}	$2.36^{+9.52}_{-2.13}$	$0.99^{+0.75}_{-0.44}$	$0.06^{+0.12}_{-0.03}$	$\log_{10} K_{Band} = 3.3^{+1.2}_{-1.7}$	
	$K_{Powerlaw}$	$1.74^{+0.23}_{-0.19} \times 10^{-2}$	$4.12^{+0.49}_{-0.41} \times 10^{-2}$	$4.35^{+0.42}_{-0.37} \times 10^{-2}$	$3.49^{+0.10}_{-0.14} \times 10^{-2}$	
	$E(B - V)_{host}$	$0.089^{+0.016}_{-0.014}$	$0.099^{+0.015}_{-0.014}$	$0.109^{+0.012}_{-0.012}$	0.106	
	BIC	125	209	251	97	
Powerlaw+BB	$N_{H,host}(10^{22}\text{cm}^{-1})$	$0.73^{+0.29}_{-0.23}$	$2.55^{+0.37}_{-0.34}$	$0.48^{+0.29}_{-0.14}$	$0.16^{+2.04}_{-0.13}$	
	kT (keV)	$172.04^{+20.81}_{-49.01}$	$1.34^{+0.07}_{-0.06}$	$0.53^{+0.06}_{-0.06}$	$3.68^{+11.47}_{-3.61}$	
	K_{BB}	$1.07^{+0.75}_{-0.73}$	$0.08^{+0.01}_{-0.01}$	$1.38^{+0.03}_{-0.04} \times 10^{-2}$	$1.86^{+1.55}_{-1.53} \times 10^{-3}$	
	α_{PL}	$1.74^{+0.02}_{-0.02}$	$1.54^{+0.07}_{-0.06}$	$1.67^{+0.03}_{-0.02}$	$1.94^{+0.02}_{-0.02}$	
	$K_{Powerlaw}$	$0.11^{+0.01}_{-0.01}$	$0.96^{+0.04}_{-0.04}$	$5.60^{+2.60}_{-4.40} \times 10^{-3}$	$0.05^{+0.01}_{-0.01}$	
	$E(B - V)_{host}$	$0.115^{+0.014}_{-0.015}$	$0.145^{+0.012}_{-0.012}$	$0.174^{+0.08}_{-0.019}$	$0.100^{+0.013}_{-0.014}$	
	BIC	123	260	296	110	
Powerlaw+SYN	p	$2.8^{+2.0}_{-0.6}$	$3.5^{+0.2}_{-0.2}$	$3.1^{+0.2}_{-0.3}$	$5.2^{+0.6}_{-1.2}$	
	$\log_{10} B(\text{G})$	$-0.24^{+0.37}_{-0.41}$	$-0.52^{+0.04}_{-0.04}$	$-1.30^{+0.08}_{-0.06}$	$-1.92^{+0.12}_{-0.06}$	
	$\log_{10} \gamma_c$	$1.25^{+0.54}_{-2.60}$	$-1.60^{+0.42}_{-0.28}$	$-1.27^{+0.63}_{-0.49}$	$0.25^{+0.63}_{-0.67}$	
	$\log_{10} \gamma_{\max}$	$-2.44^{+0.30}_{-0.36}$	$-2.54^{+0.34}_{-0.31}$	$-2.52^{+0.34}_{-0.34}$	$-2.49^{+0.34}_{-0.33}$	
	$\log_{10} K$	$-5.23^{+1.91}_{-0.52}$	$-3.51^{+0.19}_{-0.26}$	$-2.84^{+0.28}_{-0.36}$	$-2.65^{+0.43}_{-0.47}$	
	$K_{Powerlaw}$	$1.72^{+0.21}_{-0.19} \times 10^{-2}$	$3.90^{+0.40}_{-0.38} \times 10^{-2}$	$4.37^{+0.48}_{-0.44} \times 10^{-2}$	$3.41^{+0.36}_{-0.36} \times 10^{-2}$	
	$E(B - V)_{host}$	$0.094^{+0.016}_{-0.015}$	$0.094^{+0.013}_{-0.013}$	$0.109^{+0.014}_{-0.014}$	$0.113^{+0.016}_{-0.015}$	
Powerlaw	BIC	131	309	252	108	
	$N_{H,host}(10^{22}\text{cm}^{-1})$	$0.77^{+0.27}_{-0.24}$	$3.71^{+0.35}_{-0.47}$	$0.81^{+0.11}_{-0.10}$	$0.06^{+0.11}_{-0.05}$	$0.137^{+0.19}_{-0.10}$
	α_{PL}	$1.74^{+0.02}_{-0.02}$	$1.67^{+0.03}_{-0.02}$	$1.70^{+0.01}_{-0.01}$	$1.94^{+0.02}_{-0.02}$	$1.99^{+0.03}_{-0.03}$
	$K_{Powerlaw}$	$0.11^{+0.01}_{-0.01}$	$1.45^{+0.04}_{-0.04}$	$0.83^{+0.02}_{-0.02}$	$0.05^{+0.01}_{-0.01}$	$0.03^{+0.01}_{-0.01}$
	$E(B - V)_{host}$	$0.112^{+0.014}_{-0.014}$	$0.216^{+0.007}_{-0.006}$	$0.254^{+0.015}_{-0.014}$	$0.102^{+0.012}_{-0.011}$	$0.089^{+0.025}_{-0.023}$
Powerlaw	BIC	114	633	418	94	91

Table 1. Spectral Fitting Parameters for GR110801A

4. AFTERGLOW EMISSION ANALYSIS

4.1. *Temporal behavior of the afterglow*

The afterglow emission is typically characterized by power-law dependencies in both the temporal and spectral regimes with $F_\nu = t^{-\alpha} \nu^{-\beta}$. UV/optical light curves of late afterglow after $T_0 + 4000$ s were phenomenologically fitted with a simple power-law(SPL). Since the γ -ray emission from $T_0 - 50$ to $T_0 + 80$ s could be the prompt emission of the first burst, the $T_0 - 50$ s is treated as the true start time of the first burst in the afterglow modeling(i.e., the launch time of the jet). All times are given from T_0 to $T_0 + T$ unless otherwise stated. The best fitted SPL model of UV/optical light curves in WHITE, U, B, V and W1 band gives $\alpha_3 = 1.1 \pm 0.1$ for late-time afterglow. We also treat the optical data from $T_0 + 80$ to $T_0 + 1000$ s as the afterglow emission of the first burst and fit them with a smoothly broken power-law(SBPL), which has been widely used to fit afterglow light curves for both the rising and decay phases (e.g., E.-W. Liang et al. 2007; L. Li et al. 2012; X.-G. Wang et al. 2015; L.-Y. Huang et al. 2018). The SBPL can be written as :

$$f(t) = A \left[\left(\frac{t}{t_b} \right)^{\alpha_1 \Delta} + \left(\frac{t}{t_b} \right)^{\alpha_2 \Delta} \right]^{-1/\Delta} \quad (6)$$

where A is the normalization factor, t_b is the break time, α_1 and α_2 are the temporal decay indices, Δ is the smooth parameter. During the early afterglow phase, the WHITE-band light curve exhibits a steep rise with $\alpha_1 = -2.5 \pm 0.4$, while the U-band shows an even steeper rise with $\alpha_2 = -6.5^{+1.0}_{-1.3}$ after $T_0 + 250$ s, which may indicate a dominated RS

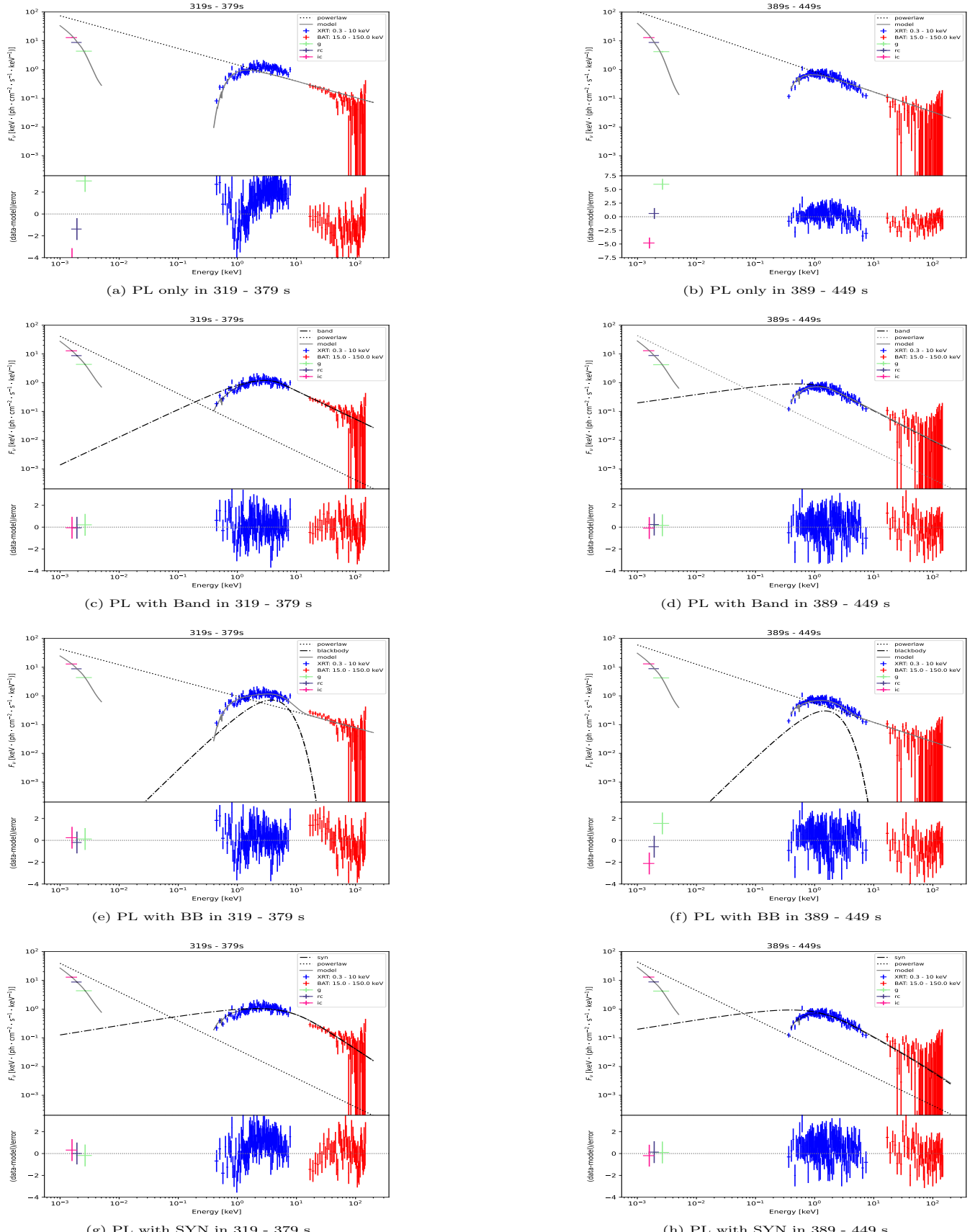


Figure 2. The SEDs of GRB 110801A prompt emission. (a)(b) PL only: spectral fitting of the 319–379 s and 389–449 s interval (PL only model). (c)(d) PL with Band: spectral fitting of the 319–379 s and 389–449 s interval (PL with Band model). (e)(f) PL with BB: spectral fitting of the 319–379 s and 389–449 s interval (PL with BB model). (g)(h) PL with SYN model: spectral fitting of the 319–379 s and 389–449 s interval (PL with SYN model). Dotted lines represent the unabsorbed PL component, dash-dot lines represent the unabsorbed Band or BB or SYN component, and the solid gray line represents the predictions generated by the model.

component along with a FS. Hence, to account for the behavior of the early afterglow in the brightening phase, both the RS and FS components should be considered.

4.2. The spectral analysis of the afterglow

The epoch from $T_0 + 4500$ to $T_0 + 58500$ s is selected to construct the broad band SED since we have the best multi-band coverage data and high SNR. The XRT data from this epoch were collected to create the X-ray spectrum. As shown above, the UVOT UV/optical light curves in the decay phase can be well described by a power-law decay with a temporal decay index $\alpha_3 = 1.1 \pm 0.1$. Hence, the UV/optical data were interpolated to $T_0 + 13400$ s with the equivalent photon arrival time of ~ 13400 s in this epoch to fit the broad-band SEDs. Due to being potentially affected by Lyman- α and the Lyman limit in the UVW1 and U bands, and the uncertainty in defining the effective wavelength of the broad WHITE band, we utilized only the V and B bands for SED fitting. The V and B band fluxes used to construct the SEDs are 1.16×10^{-4} Jy and 7.92×10^{-5} Jy, respectively, with adopted uncertainties of 10%.

The broad band SED was fitted with an absorbed PL model $F_\nu \propto \nu^{-\beta}$. The Milky Way extinction model with $E(B - V)_{\text{MW}} = 0.0693$ (E. L. Fitzpatrick 1999) and $R_V = 3.08$ is adopted. For the host, the extinction model of the Small Magellanic Cloud model is adopted. The best fitted result gives the spectral index $\beta = 2.00 \pm 0.05$, the $E(B - V)_{\text{host}}$ of the host galaxy is 0.07 ± 0.03 and the equivalent hydrogen column density of the host galaxy $N_{\text{H,host}} = 4.9_{-1.9}^{+2.0} \times 10^{21} \text{ cm}^{-2}$ which is shown in Figure 3.

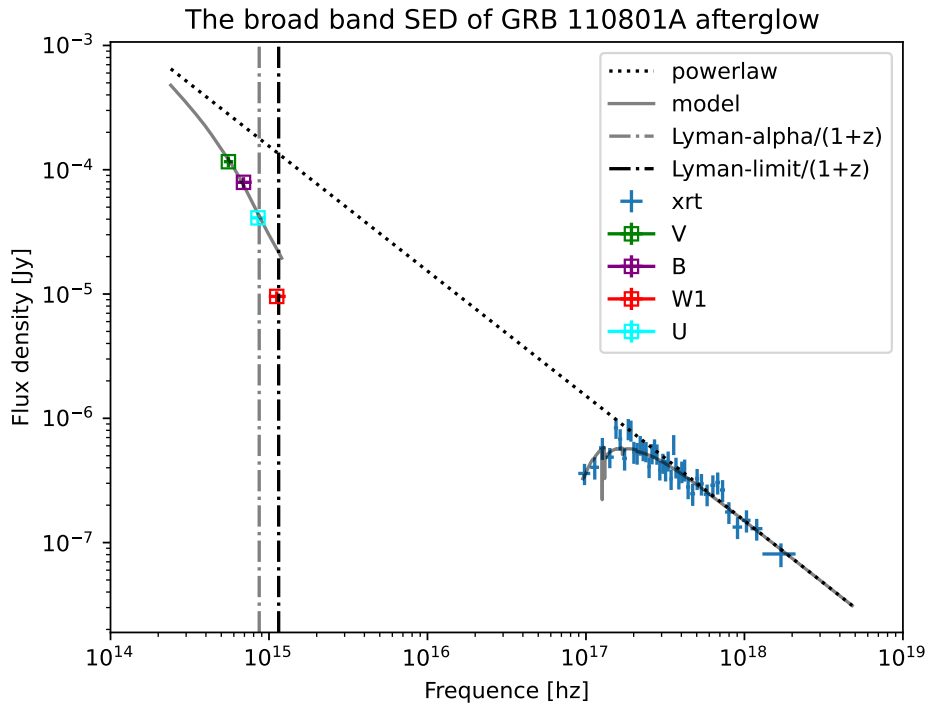


Figure 3. The broad band SED of GRB 110801A afterglow from $T_0 + 4500$ to $T_0 + 58500$ s with the equivalent photon arrival time of ~ 13400 s after the BAT trigger. Blue points are observed data of XRT from 0.3 keV to 10.0 keV. Colorful points are the observed data in different UV/optical bands. Gray solid lines represent the predicted absorbed model. Gray and black dash-dot lines represent Lyman- α and Lyman-limit lines. Dashed line is the unabsorbed power-law model with a spectral index of 2.00.

During the XSPEC fitting, the *tbabs* and *ztbabs* models are set the same as mentioned above. We attempted to fit the data with both SPL and CPL model; however, we cannot use the CPL model here because the cutoff is above the X-ray band and we do not have γ -ray band detection at this epoch.

4.3. Afterglow modeling

In the double-burst scenario, the optical light curve is characterized by a steep rise to a peak around $T_0 + 378$ s corresponding to the afterglow of the first burst. The beginning of steep optical rise is not observed by the UVOT,

but it can be constrained that the rise starts before the first observation at $T_0 + 135$ s in the WHITE band. The steep rise observed in the light curve during the transition from the WHITE band to the U band at $T_0 + 278$ s can constrain the onset of the RS. The peak reaches $U = 16.6$ AB mag and following the peak, UV/optical light curves decay monotonically without significant color evolution. After 7×10^4 s, a further steepening break in g, Rc and Ic band is observed, probably caused by a jet break.

Meanwhile, the X-ray data show a different temporal behavior. The X-ray light curve begins to rise at $T_0 + 320$ s, consistent with the behavior of the γ -rays. However, this is different from the optical evolution, which shows an onset at $T_0 + 135$ s in the WHITE band and a steep rise at $T_0 + 278$ s in the U band. After the peak around $T_0 + 380$ s, the X-ray light curve shows a monotonic decay and turns into a normal decay with a temporal index of -1.2 at late-time which is similar to optical decay. Subsequently, after 10^5 s, a comparable break also appears, likely attributed to a jet break seen in the optical bands.

As the relativistic outflow of the GRB propagates into the circumburst medium, it drives a pair of relativistic shocks, i.e., FS and RS components. Initially, the light curve is dominated by the FS emission characterized by an onset in the WHITE band. The RS soon takes over, characterized by a steep rise in the U band. After the peak in the U band, FS dominates the decay phase. The electrons accelerated by relativistic shocks are capable of producing multi-band emissions via synchrotron radiation and inverse Compton scattering. Numerous computational paradigms for modeling afterglows have been developed. To perform numerical calculations of the radiation contributed from the FS component under the various effects, we use a Python-wrapped FORTRAN package⁶(J. Ren et al. 2024). For the calculation of the contribution from the RS in the early afterglow phase, it is referenced from (S.-X. Yi et al. 2013). Therefore, in this model, the flux density at a certain time and frequency is:

$$F_{t,\nu} = F(t, \nu, \Gamma_0, \epsilon_{e,f}, \epsilon_{B,f}, \theta_j, E_{k,iso}, p_f, \epsilon_{e,r}, \epsilon_{B,r}, p_r, n_0, f_e), \quad (7)$$

where Γ_0 is the initial Lorentz factor, ϵ_e is the fraction of the shock energy converted into the energy of relativistic electrons, ϵ_b is the fraction of the shock energy converted into the energy of magnetic field, θ_j is the half-opening angle of the jet in radians, $E_{k,iso}$ is the isotropic kinetic energy of the jet, p is the electron energy distribution index, n_0 is the number density of the circumburst medium. And the additional subscripts f and r represent the FS and RS, respectively.

We utilize `emcee` (D. Foreman-Mackey et al. 2013) to conduct Bayesian inference on the parameters of the afterglow model (Eq. 7). The prior ranges for these parameters are provided in Table 3. We consider a γ -ray radiation efficiency $\eta_\gamma > 0.1\%$ (the minimum value reported in the statistical study by B. Zhang et al. (2007)), which corresponds to an upper bound of 55 for the prior of $\log_{10} E_{k,iso}$. Furthermore, we introduce a log-likelihood term. For a given data point at time t_i in a band with central frequency ν_i , the log-likelihood is calculated:

$$\ln \mathcal{L}_i = -\frac{1}{2} \frac{(F_{t,\nu} - F_{t,\nu,obs})^2}{\sigma_i^2 + f_{sys}^2 F_{t,\nu,obs}^2}. \quad (8)$$

where f_{sys} is a free parameter to characterize the systematic error. Furthermore, considering the difficulty in accurately calculating the extinction for the WHITE, U, and W1 bands, we introduced a free parameter to the magnitudes of each of these three bands. In the double-burst scenario, the first ejecta initially propagate through the medium while decelerating. The second ejecta, launched approximately during the active phase of the second pulse, moves at a constant velocity because the first ejecta has already swept up most of the ambient material. Consequently, it eventually catches up and collides with the first ejecta. By interpolating the numerical calculation results for the radius evolution of the first ejecta, we derive that the second ejecta, moving at a constant velocity, would catch up with the first ejecta approximately 370 s in the observer frame. We model the energy extraction from the catch-up result as a continuous energy injection in the form of $L(t) = L_0(\frac{t}{t_1})^{-q}$, where q is the energy injection index (Z. G. Dai & T. Lu 1998; B. Zhang & P. Mészáros 2001; B. Zhang et al. 2006). Here we adopt the radiation efficiency of 10% ($L_0 \sim 10^{51} \text{ erg} \cdot \text{cm}^{-2} \cdot \text{s}^{-1}$), and $q = 2$ as typical values. The best simultaneous fit results are shown in Figure 4 and the parameters are summarized in Figure 5. By fitting the light curves, we are able to constrain various parameters for both the FS and RS components. According to the FS and RS models, the modeled light curves reproduce both the multi-band optical data and the late-time X-ray emission well, with all derived parameters constrained within typical

⁶ https://github.com/mikuru1096/ASGARD_GRBAfterglow

ranges. This consistency corroborates the hypothesis suggested by our joint spectral fitting that the optical emission is dominated by the afterglow contribution of the first burst. Furthermore, the initial Lorentz factor $\Gamma_0 \sim 60$, the half-opening angle $\theta_0 \sim 0.09$ and the isotropic kinetic energy $E_{k,iso} \sim 10^{54.8}$ erg. The fit result constrains well the fraction of the forward shock energy converted into the energy of magnetic field $\epsilon_{B,f} = 2.6 \times 10^{-3}$ and the reverse shock energy converted into the energy of magnetic field $\epsilon_{B,r} = 2.0 \times 10^{-4}$.

5. SUMMARY AND DISCUSSION

We presented a detailed analysis of the prompt emission and the early afterglow of GRB 110801A, and suggest GRB 110801A is a double-burst GRB triggered by its first burst in γ -ray emission. Initially, a pulse in the γ -ray band triggered the BAT. Approximately 130 s after the trigger, the optical light curve began to rise. This onset preceded the second pulse observed in both X-ray and γ -ray bands, where the flux in the γ -ray band of the second pulse was comparable to that of the first. These features suggest the presence of two distinct burst episodes. The optical band exhibited a significant change in its temporal behavior. If we assume $T_0 - 50$ s as the true onset of the burst, the temporal index of the optical rise steepened from -2.5 to -6.5 between $T_0 + 230$ s and $T_0 + 280$ s. Such a transition and rapid rise are attributed to the contribution of the reverse shock of the afterglow. After 1000 s, both the UV/optical and X-ray light curves show normal decay behaviors. We summarize our main results as follows:

(i) According to simultaneous multi-band observation, we find that GRB 110801A exhibits two comparable bursts in the γ -ray band before and after the trigger, implying that it may be a double-burst event. The temporal discrepancy between the early optical brightening and the delayed rising in the X-ray/ γ -ray band points to different physical origins. This is consistent with previous literature, where chromatic behaviors between optical and X-ray bands are often observed (A. K. Ror et al. 2025). The comprehensive data of GRB 110801A make it possible to study the mechanisms of emission and to constrain several parameters of the standard fireball model.

(ii) After the first burst, the *Swift*/XRT, *Swift*/BAT and OAO data were jointly fitted. We find that an additional Band component is required to account for the excess in the X-ray and γ -ray bands, and the optical emission can be attributed to a power-law component. Moreover, by constraining the power-law parameters based on the late-time afterglow data, we obtained a reasonable fit. This result indicates that the optical radiation likely originates from the afterglow of the first burst, whereas the X-ray and γ -ray emissions are more likely associated with the prompt emission of the second burst in the framework of synchrotron mechanism.

(iii) Considering the transition from a normal rise($\sim t^{2.5}$) to a steep rise($\sim t^{6.5}$) observed in the WHITE and U bands, we adopt the scenario that both the RS and the FS contribute considerably to the afterglow at the early stage. Due to well-sampled data of the afterglow in the early phase, some physical parameters of RS and FS can be well constrained. The best fitted model shows that the UV/optical light curves are initially dominated by the RS and the FS takes over after $\sim T_0 + 378$ s. From RS and FS modeling, we have the initial Lorentz factor $\Gamma_0 \sim 60$, the half-opening angle $\theta_j \sim 0.09$, isotropic kinetic energy $E_{k,iso} \sim 10^{54.8}$ erg, and $\mathcal{R}_B = (\epsilon_{B,r}/\epsilon_{B,f})^{\frac{1}{2}} \approx 0.08$.

In conclusion, with the broadband coverage and high temporal resolution of double-burst GRB 110801A, our analysis reveals that the pulse in the X-ray and γ -ray bands at approximately 320 s originates from internal shocks of the second burst, while the rapid rise in the optical band originates from the external shock of the first burst and their parameters are constrained.

ACKNOWLEDGMENTS

We acknowledge the use of the public data from the Swift archive. This work is supported by the National Key R&D Program of China (grant Nos. 2024YFA1611704 and 2024YFA1611700), the Natural Science Foundation of China (grant Nos. 12225305, 12473049, 12321003, and 12233011), the Strategic Priority Research Program of the Chinese Academy of Sciences (grant No. XDB0550400), the Jiangsu Funding Program for Excellent Postdoctoral Talent (grant No. 2024ZB110), the Basic Research Program of Jiangsu (grant No. BK20251707), the Postdoctoral Innovation Talents Support Program (No. BX20250159), the Postdoctoral Fellowship Program (grant No. GZC20241916), and the General Fund (grant No. 2024M763531) of the China Postdoctoral Science Foundation.

Facilities: Swift(BAT, XRT and UVOT)

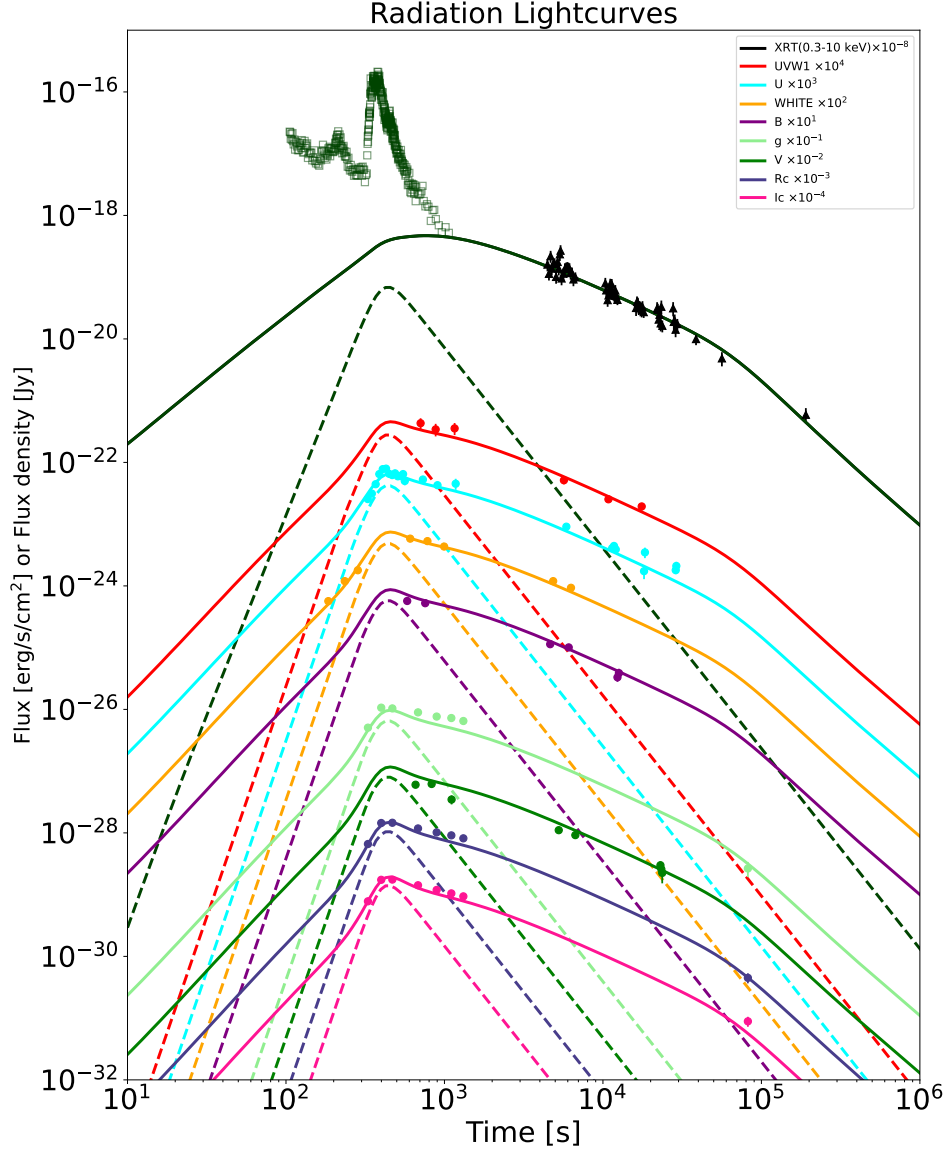


Figure 4. GRB 110801A light curves from XRT, UVOT and OAO data. In this scenario, we consider the optical peak as dominated by RS. The open squares represent XRT data excluded from afterglow fitting. Dashed line represents the RS contribution while solid line represents the sum contribution of all components.

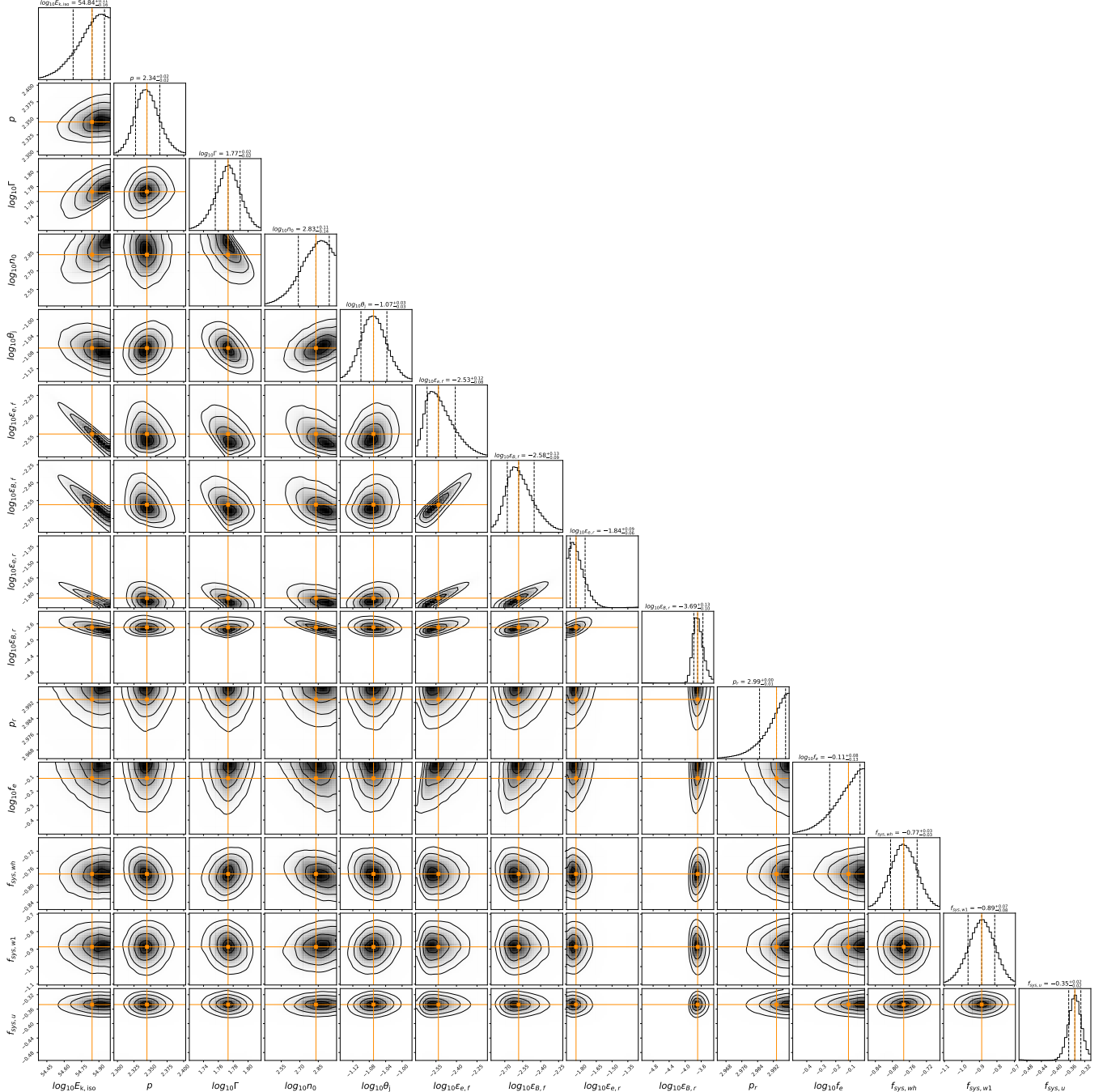


Figure 5. Constrained parameters of the afterglow model for GRB 110801A. Here Γ_0 is the initial Lorentz factor, ϵ_e is fraction of energy of relativistic electrons, ϵ_b is fraction of the energy of magnetic field, θ_j is the half-opening angle in radians, $E_{k,\text{iso}}$ is the isotropic kinetic energy, p is the electron energy distribution index, n_0 is the medium number density. And the additional subscripts f and r represent the FS and RS, respectively. $f_{\text{sys},\text{wh}}$, $f_{\text{sys},\text{w1}}$ and $f_{\text{sys},u}$ are the free parameters to the magnitudes.

APPENDIX

In this appendix, we provide detailed information on the observation data and fitting results of the parameters in the prompt and afterglow phases.

Table 2. *Swift* UVOT photometric observation

$T - T_0$ (s)	Exposure(s)	Magnitude	Error	Filter
135	50	19.62	0.15	WHITE
185	50	18.81	0.08	WHITE
234	50	18.37	0.07	WHITE
278	20	17.78	0.15	U
298	20	17.56	0.13	U
318	20	17.18	0.11	U
338	20	16.77	0.09	U
358	20	16.57	0.08	U
378	20	16.55	0.08	U
398	20	16.76	0.09	U
418	20	16.81	0.09	U
438	20	16.74	0.09	U
458	20	16.86	0.10	U
478	20	16.85	0.10	U
498	20	16.77	0.09	U
512	8	17.05	0.16	U
532	20	16.09	0.09	B
558	20	17.09	0.06	WHITE
607	20	15.64	0.12	V
657	20	18.28	0.22	UVW1
681	20	16.99	0.11	U
706	20	16.18	0.09	B
731	20	17.19	0.06	WHITE
780	20	15.61	0.12	V
830	20	18.53	0.25	UVW1
854	20	17.22	0.13	U
945	150	17.41	0.03	WHITE
1059	20	16.24	0.18	V
1109	18	18.49	0.24	UVW1
1127	6	17.16	0.22	U
4597	197	17.43	0.05	B
4802	197	18.33	0.03	WHITE
5212	197	17.18	0.08	V
5622	197	19.93	0.15	UVW1
5827	197	18.36	0.07	U
6032	197	17.56	0.07	B
6237	197	18.60	0.04	WHITE
6648	197	17.38	0.14	V
10782	886	20.70	0.11	UVW1
11389	295	19.23	0.08	U
11692	295	19.14	0.09	U

$T - T_0$ (s)	Exposure(s)	Magnitude	Error	Filter
11996	295	19.28	0.12	U
12301	295	18.77	0.17	B
12565	218	18.60	0.19	B
17515	886	20.99	0.15	UVW1
18121	295	20.16	0.28	U
18361	171	19.40	0.21	U
23009	295	18.60	0.17	V
23313	295	18.76	0.23	V
23616	295	18.91	0.35	V
28747	295	20.12	0.15	U
29002	200	19.95	0.18	U

End of the Table

Note. The photometry results presented in this table have not been corrected for Galactic extinction.

Table 3. Fitting results of model parameters

Parameter	Prior range	Posterior value
$\log_{10} \Gamma_0$	[1, 2.5]	$1.77^{+0.02}_{-0.02}$
$\log_{10} \epsilon_{e,f}$	[-3, -0.1]	$-2.53^{+0.12}_{-0.08}$
$\log_{10} \epsilon_{B,f}$	[-7, -0.1]	$-2.58^{+0.13}_{-0.09}$
$\log_{10} \theta_j$ (rad)	[-2, 0]	$-1.07^{+0.03}_{-0.03}$
$\log_{10} E_{k,\text{iso}}$ (erg)	[51, 55]	$54.84^{+0.11}_{-0.16}$
p_f	[2, 3]	$2.34^{+0.02}_{-0.02}$
$\log_{10} \epsilon_{e,r}$	[-3, -0.1]	$-1.84^{+0.09}_{-0.06}$
$\log_{10} \epsilon_{B,r}$	[-7, -0.1]	$-3.69^{+0.13}_{-0.10}$
p_r	[2, 3]	$2.99^{+0.00}_{-0.01}$
$\log_{10} n_0$	[-3, 3]	$2.83^{+0.11}_{-0.14}$
$\log_{10} f_e$	[-3, 0]	$-0.11^{+0.08}_{-0.13}$
$f_{\text{sys},wh}$	[-3, 3]	$-0.77^{+0.03}_{-0.03}$
$f_{\text{sys},w1}$	[-3, 3]	$-0.89^{+0.07}_{-0.08}$
$f_{\text{sys},u}$	[-3, 3]	$-0.35^{+0.02}_{-0.02}$

^a Uniform prior distribution.

^b The confidence interval is set to 1σ .

REFERENCES

Abbott, B. P., Abbott, R., Abbott, T. D., et al. 2017, The Astrophysical Journal Letters, 848, L12, doi: [10.3847/2041-8213/aa91c9](https://doi.org/10.3847/2041-8213/aa91c9)

Arimoto, M., Asano, K., Kawabata, K. S., et al. 2024, Nature Astronomy, 8, 134, doi: [10.1038/s41550-023-02119-1](https://doi.org/10.1038/s41550-023-02119-1)

Band, D., Matteson, J., Ford, L., et al. 1993, ApJ, 413, 281, doi: [10.1086/172995](https://doi.org/10.1086/172995)

Barthelmy, S. D., Barbier, L. M., Cummings, J. R., et al. 2005, Space Science Reviews, 120, 143, doi: [10.1007/s11214-005-5096-3](https://doi.org/10.1007/s11214-005-5096-3)

Beniamini, P., & Granot, J. 2016, MNRAS, 459, 3635, doi: [10.1093/mnras/stw895](https://doi.org/10.1093/mnras/stw895)

Blake, C. H., Bloom, J. S., Starr, D. L., et al. 2005, Nature, 435, 181, doi: [10.1038/nature03520](https://doi.org/10.1038/nature03520)

Burgess, J. M., Bégué, D., Greiner, J., et al. 2020, Nature Astronomy, 4, 174, doi: [10.1038/s41550-019-0911-z](https://doi.org/10.1038/s41550-019-0911-z)

Burlon, D., Ghirlanda, G., Ghisellini, G., et al. 2008, ApJL, 685, L19, doi: [10.1086/592350](https://doi.org/10.1086/592350)

Burrows, D. N., Hill, J. E., Nousek, J. A., et al. 2005, Space Science Reviews, 120, 165, doi: [10.1007/s11214-005-5097-2](https://doi.org/10.1007/s11214-005-5097-2)

Cabrera Lavers, A., de Ugarte Postigo, A., Castro-Tirado, A. J., et al. 2011, GRB Coordinates Network, 12234, 1

Dai, Z. G., & Lu, T. 1998, *A&A*, 333, L87, doi: [10.48550/arXiv.astro-ph/9810402](https://doi.org/10.48550/arXiv.astro-ph/9810402)

Daigne, F., Bošnjak, Ž., & Dubus, G. 2011, *A&A*, 526, A110, doi: [10.1051/0004-6361/201015457](https://doi.org/10.1051/0004-6361/201015457)

de Pasquale, M., Barthelmy, S. D., Baumgartner, W. H., et al. 2011, GRB Coordinates Network, 12228, 1

Elliott, J., Yu, H. F., Schmidl, S., et al. 2014, *A&A*, 562, A100, doi: [10.1051/0004-6361/201322600](https://doi.org/10.1051/0004-6361/201322600)

Evans, P. A., Beardmore, A. P., Page, K. L., et al. 2007, *A&A*, 469, 379, doi: [10.1051/0004-6361:20077530](https://doi.org/10.1051/0004-6361:20077530)

Evans, P. A., Beardmore, A. P., Page, K. L., et al. 2009, *Monthly Notices of the Royal Astronomical Society*, 397, 1177, doi: [10.1111/j.1365-2966.2009.14913.x](https://doi.org/10.1111/j.1365-2966.2009.14913.x)

Fitzpatrick, E. L. 1999, *PASP*, 111, 63, doi: [10.1086/316293](https://doi.org/10.1086/316293)

Foreman-Mackey, D., Hogg, D. W., Lang, D., & Goodman, J. 2013, *PASP*, 125, 306, doi: [10.1086/670067](https://doi.org/10.1086/670067)

Gehrels, N., Chincarini, G., Giommi, P., et al. 2004, *The Astrophysical Journal*, 611, 1005, doi: [10.1086/422091](https://doi.org/10.1086/422091)

Gendre, B., Atteia, J. L., Boér, M., et al. 2012, *ApJ*, 748, 59, doi: [10.1088/0004-637X/748/1/59](https://doi.org/10.1088/0004-637X/748/1/59)

Ghisellini, G., Celotti, A., & Lazzati, D. 2000, *Monthly Notices of the Royal Astronomical Society*, 313, L1, doi: [10.1046/j.1365-8711.2000.03354.x](https://doi.org/10.1046/j.1365-8711.2000.03354.x)

Golkhou, V. Z., Butler, N. R., & Littlejohns, O. M. 2015, *ApJ*, 811, 93, doi: [10.1088/0004-637X/811/2/93](https://doi.org/10.1088/0004-637X/811/2/93)

Granot, J. 2016, *ApJL*, 816, L20, doi: [10.3847/2041-8205/816/2/L20](https://doi.org/10.3847/2041-8205/816/2/L20)

Guiriec, S., Connaughton, V., Briggs, M. S., et al. 2011, *ApJL*, 727, L33, doi: [10.1088/2041-8205/727/2/L33](https://doi.org/10.1088/2041-8205/727/2/L33)

Hu, Y.-D., Liang, E.-W., Xi, S.-Q., et al. 2014, *ApJ*, 789, 145, doi: [10.1088/0004-637X/789/2/145](https://doi.org/10.1088/0004-637X/789/2/145)

Huang, L.-Y., Wang, X.-G., Zheng, W., et al. 2018, *ApJ*, 859, 163, doi: [10.3847/1538-4357/aa8a6e](https://doi.org/10.3847/1538-4357/aa8a6e)

Jin, Z.-P., Zhou, H., Wang, Y., et al. 2023, *Nature Astronomy*, 7, 1108, doi: [10.1038/s41550-023-02005-w](https://doi.org/10.1038/s41550-023-02005-w)

Kobayashi, S., Piran, T., & Sari, R. 1997, *The Astrophysical Journal*, 490, 92, doi: [10.1086/512791](https://doi.org/10.1086/512791)

Komesh, T., Grossan, B., Maksut, Z., et al. 2023, *Monthly Notices of the Royal Astronomical Society*, 520, 6104, doi: [10.1093/mnras/stad538](https://doi.org/10.1093/mnras/stad538)

Koshut, T. M., Kouveliotou, C., Paciesas, W. S., et al. 1995, *ApJ*, 452, 145, doi: [10.1086/176286](https://doi.org/10.1086/176286)

Kuroda, D., Hanayama, H., Miyaji, T., et al. 2011, GRB Coordinates Network, 12233, 1

Lamb, G. P., Levan, A. J., & Tanvir, N. R. 2020, *ApJ*, 899, 105, doi: [10.3847/1538-4357/aba75a](https://doi.org/10.3847/1538-4357/aba75a)

Li, L., Liang, E.-W., Tang, Q.-W., et al. 2012, *ApJ*, 758, 27, doi: [10.1088/0004-637X/758/1/27](https://doi.org/10.1088/0004-637X/758/1/27)

Liang, E.-W., Zhang, B.-B., & Zhang, B. 2007, *ApJ*, 670, 565, doi: [10.1086/521870](https://doi.org/10.1086/521870)

Mészáros, P., & Rees, M. J. 1997, *ApJ*, 476, 232, doi: [10.1086/303625](https://doi.org/10.1086/303625)

Mészáros, P., & Rees, M. J. 1999, *MNRAS*, 306, L39, doi: [10.1046/j.1365-8711.1999.02800.x](https://doi.org/10.1046/j.1365-8711.1999.02800.x)

Moss, M. J., Mochkovitch, R., Daigne, F., Beniamini, P., & Guiriec, S. 2023, *MNRAS*, 525, 5224, doi: [10.1093/mnras/stad2594](https://doi.org/10.1093/mnras/stad2594)

Nakar, E., Ando, S., & Sari, R. 2009, *ApJ*, 703, 675, doi: [10.1088/0004-637X/703/1/675](https://doi.org/10.1088/0004-637X/703/1/675)

Pe'er, A., & Zhang, B. 2006, *ApJ*, 653, 454, doi: [10.1086/508681](https://doi.org/10.1086/508681)

Peng, F.-K., Liang, E.-W., Wang, X.-Y., et al. 2014, *ApJ*, 795, 155, doi: [10.1088/0004-637X/795/2/155](https://doi.org/10.1088/0004-637X/795/2/155)

Piran, T. 2005, *Rev. Mod. Phys.*, 76, 1143, doi: [10.1103/RevModPhys.76.1143](https://doi.org/10.1103/RevModPhys.76.1143)

Planck Collaboration, Aghanim, N., Akrami, Y., et al. 2020, *A&A*, 641, A6, doi: [10.1051/0004-6361/201833910](https://doi.org/10.1051/0004-6361/201833910)

Rees, M. J., & Meszaros, P. 1994, *ApJL*, 430, L93, doi: [10.1086/187446](https://doi.org/10.1086/187446)

Ren, J., Wang, Y., & Dai, Z.-G. 2024, *ApJ*, 962, 115, doi: [10.3847/1538-4357/ad1bcd](https://doi.org/10.3847/1538-4357/ad1bcd)

Roming, P. W. A., Kennedy, T. E., Mason, K. O., et al. 2005, *Space Sci Rev*, 120, 95, doi: [10.1007/s11214-005-5095-4](https://doi.org/10.1007/s11214-005-5095-4)

Ror, A. K., Pandey, S. B., Oates, S. R., et al. 2025, *MNRAS*, 543, 2404, doi: [10.1093/mnras/staf1514](https://doi.org/10.1093/mnras/staf1514)

Sakamoto, T., Barthelmy, S. D., Baumgartner, W., et al. 2011, GRB Coordinates Network, 12276, 1

Salafia, O. S., & Ghirlanda, G. 2022, *Galaxies*, 10, 93, doi: [10.3390/galaxies10050093](https://doi.org/10.3390/galaxies10050093)

Sari, R., & Piran, T. 1999, *ApJL*, 517, L109, doi: [10.1086/312039](https://doi.org/10.1086/312039)

Schroeder, G., Rhodes, L., Laskar, T., et al. 2024, *ApJ*, 970, 139, doi: [10.3847/1538-4357/ad49ab](https://doi.org/10.3847/1538-4357/ad49ab)

Schwarz, G. 1978, *The annals of statistics*, 461

Sun, T.-R., Geng, J.-J., Yan, J.-Z., et al. 2024, *ApJL*, 976, L20, doi: [10.3847/2041-8213/ad85da](https://doi.org/10.3847/2041-8213/ad85da)

Troja, E., Lipunov, V. M., Mundell, C. G., et al. 2017, *Nature*, 547, 425, doi: [10.1038/nature23289](https://doi.org/10.1038/nature23289)

Uhm, Z. L., & Zhang, B. 2014, *Nature Physics*, 10, 351, doi: [10.1038/nphys2932](https://doi.org/10.1038/nphys2932)

Valan, V., & Larsson, J. 2021, *MNRAS*, 501, 4974, doi: [10.1093/mnras/staa3978](https://doi.org/10.1093/mnras/staa3978)

Vianello, G., Gill, R., Granot, J., et al. 2018, *ApJ*, 864, 163, doi: [10.3847/1538-4357/aad6ea](https://doi.org/10.3847/1538-4357/aad6ea)

Wang, H., Zhou, H., Fan, Y.-Z., & Wei, D.-M. 2025, *ApJ*, 990, 110, doi: [10.3847/1538-4357/adf1a2](https://doi.org/10.3847/1538-4357/adf1a2)

Wang, Q.-L., Zhou, H., Wang, Y., et al. 2025, ApJ, 987, 129, doi: [10.3847/1538-4357/add693](https://doi.org/10.3847/1538-4357/add693)

Wang, X.-G., Zhang, B., Liang, E.-W., et al. 2015, ApJS, 219, 9, doi: [10.1088/0067-0049/219/1/9](https://doi.org/10.1088/0067-0049/219/1/9)

Willingale, R., Starling, R. L. C., Beardmore, A. P., Tanvir, N. R., & O'Brien, P. T. 2013, MNRAS, 431, 394, doi: [10.1093/mnras/stt175](https://doi.org/10.1093/mnras/stt175)

Woosley, S., & Bloom, J. 2006, Annual Review of Astronomy and Astrophysics, 44, 507, doi: <https://doi.org/10.1146/annurev.astro.43.072103.150558>

Yi, S.-X., Wu, X.-F., & Dai, Z.-G. 2013, ApJ, 776, 120, doi: [10.1088/0004-637X/776/2/120](https://doi.org/10.1088/0004-637X/776/2/120)

Zhang, B., Fan, Y. Z., Dyks, J., et al. 2006, ApJ, 642, 354, doi: [10.1086/500723](https://doi.org/10.1086/500723)

Zhang, B., & Mészáros, P. 2001, ApJL, 552, L35, doi: [10.1086/320255](https://doi.org/10.1086/320255)

Zhang, B., Liang, E., Page, K. L., et al. 2007, ApJ, 655, 989, doi: [10.1086/510110](https://doi.org/10.1086/510110)

Zhang, B.-B., Burrows, D. N., Zhang, B., et al. 2012, ApJ, 748, 132, doi: [10.1088/0004-637X/748/2/132](https://doi.org/10.1088/0004-637X/748/2/132)

Zhao, X., Li, Z., Liu, X., et al. 2014, ApJ, 780, 12, doi: [10.1088/0004-637X/780/1/12](https://doi.org/10.1088/0004-637X/780/1/12)

Zhou, H., Jin, Z.-P., Covino, S., Fan, Y.-Z., & Wei, D.-M. 2023, ApJS, 268, 65, doi: [10.3847/1538-4365/acf20a](https://doi.org/10.3847/1538-4365/acf20a)